Full length article

Precipitate formation in aluminium alloys: Multi-scale modelling approach

David Kleiven[a,*], Jaakko Akola[a,b]

[a] Department of Physics, Norwegian University of Science and Technology (NTNU), Trondheim NO-7491, Norway
[b] Computational Physics Laboratory, Tampere University, P.O. Box 692, Tampere FI-33014, Finland

A R T I C L E   I N F O

A B S T R A C T

Ternary Al−Mg−Si alloys have been modelled based on a multi-scale approach that spans across atomistic and mesoscale models and uses theoretically determined parameters. First, a cluster expansion model for total energy has been trained for atomistic configurations (FCC lattice) based on the data from density functional simulations of electronic structure. Free energy curves as a function of solute (Mg, Si) concentrations and disorder have been obtained by using this parameterisation together with meta-dynamics Monte Carlo sampling. In addition, free energy data, surface tensions as well as strain energy using the linear elasticity theory have been collected to be combined for a mesoscale phase-field model. The application of this approach shows that the formation of a layered MgSi phase, with (100) planes, is a particularly stable solute aggregation motif within the Al host matrix. Moreover, the phase-field model demonstrates that the preferred shape of the MgSi precipitates is needle-like (in FCC), and they can act as precursors for the important and well-known β''-type precipitates which are formed by translating one Mg column by a 1/2 lattice vector. The results provide theoretical evidence that the solute aggregation into needle-like MgSi domains (precipitates) is an inherent property of Al-Mg-Si alloys, and that it takes place even without the presence of vacancies which is a precondition for the eventual formation β'' precipitates.

1. Introduction

Aluminium alloys have important applications in a variety of industries [1,2]. Alloys with numerous combinations of solute elements are commercially available today, and among these Al−Mg−Si (6xxx-series) is a particularly popular alloy system due to its beneficial mechanical properties [3,4]. For the 6xxx-series, the main function of the solute elements is to strengthen the material by forming meta-stable needle-like precipitates. The manufacturing process starts at high temperatures (below the melting point) with a supersaturated solid solution. The material is then rapidly cooled down to room temperature to obtain a starting structure for ageing treatment with well-dispersed solute atoms and vacancies. During ageing, the quenched material is heated by a few hundred degrees (e.g. up to 195℃) within an extended period of time to enable the solute species to diffuse and form precipitates, being assisted by the presence of vacancies. While the precipitate phases of this alloy system have been investigated thoroughly experimentally, there is a timely need for theoretical multi-scale models to study and understand their formation mechanisms in detail.

In this work, we report simulations of Al−Mg−Si alloys and their thermodynamics by using the cluster expansion (CE) formalism [5] where the parameters have been trained by fitting configurational energy data from density functional theory (DFT) simulations. The CE method has emerged as a valuable tool for identifying stable phases [6−8] and studying nucleation mechanisms in crystalline alloys [9−11]. Although alternative computational methods such as neural network potentials [12] exist for Al−Mg−Si, the CE method is applied as it typically requires less training data. Hence, for systems that are well described by a lattice model, CE is a more efficient choice. Here, the nucleation process towards the needle-like β''-precipitate is of particularly high interest due to its strengthening effect within the Al host material [13]. During the thermal ageing process, solute atoms diffuse and form Guinier−Preston (GP) zones, which further develop to the bespoke precipitates. The GP zones often have a crystal structure that matches that of the host material (here, FCC). Hence, lattice-based methods, such as CE in combination with Monte Carlo (MC), are well suited to study GP zone formation.

Long-range elastic fields will become present as GP zones form in the host material because of a lattice mismatch between the two phases. While DFT-trained CE is ideal for capturing short-range interactions

 * Corresponding author.
 E-mail addresses: david.kleiven@ntnu.no (D. Kleiven), jaakko.akola@ntnu.no (J. Akola).

(atomic configurations), the long-ranged nature of the elastic fields is hard to incorporate as this would require DFT calculations of very large atomic models. An alternative approach is to apply phase-field methods where elastic fields can be accounted for in a straightforward manner [14−18]. Here, we combine DFT, CE-MC and phase-field methods in a multi-scale approach, thereby utilising the strengths of the three approaches at different length scales. We use DFT for computing configurational, interfacial and elastic energies, CE-MC to simulate local free energy densities, and then we add this information together with the strain effects from the linear elasticity theory to a phase-field model. As a result of the phase-field simulations, we demonstrate the formation of needle-like precipitates in mesoscale and show that their formation is an inherent property of the material that can take place even without the presence of vacancies (experimental condition). We remark that the whole model development chain starts from first-principles as the underlying parameters have been computed via DFT.

2. Theory

In the cluster expansion (CE) formalism, the total energy of an atomic configuration is expanded in a set of correlation functions [5,19]. Each cluster type contributes by an effective cluster interaction (ECI) to the total energy of an atomic configuration. A selection of clusters is shown in Fig. 1. Mathematically, the total energy is described by

$$E(\boldsymbol{\sigma}) = \sum_{c_f} \sum_{d} V_{c_f}^{(d)} \langle \prod_{i \in c_f} \phi_{d_i}(\sigma_i) \rangle, \tag{1}$$

where c_f denotes a set of sites in a many-body cluster, d is a set of decoration numbers and $V_{c_f}^{(d)}$ is the effective cluster interaction, ϕ_{d_i} is a single site basis function and σ_i is an occupation variable that is unique for each atomic species. The average ($\langle \cdots \rangle$) is taken over all clusters that are mutually symmetrically equivalent.

For the ternary Al−Mg−Si system, we use the basis functions

$$\begin{aligned} \phi_0 &= 1 \\ \phi_1 &= \sqrt{\frac{3}{2}}\sigma_i \\ \phi_2 &= \sqrt{\frac{3}{2}}\left(\sigma_i^2 - \frac{2}{3}\right) \end{aligned} \tag{2}$$

The occupation variable σ_i takes the values $\{-1, 0, 1\}$ if site i is occupied by Al, Mg or Si, respectively. The ECI values are determined from fits to the training data, obtained by DFT calculations of Al-Mg-Si structures. In the present study, all clusters up to 4 atoms and a maximum diameter of 5Å were included. To avoid overfitting, a sparse energy model was constructed using $L1$ regularised fits [20].

The rest of the theory section is organised as follows: First, we explain the Monte Carlo sampling strategy that we employ to obtain free energy data. After that, we discuss aspects of the phase-field modelling, and finally, we explain the link between DFT, free energy from MC sampling and gradient coefficients needed for the phase-field model. An overview of the entire multi-scale method hierarchy is shown in Fig. 2.

2.1. Monte Carlo sampling

The parameterised energy model in Eq. (1) can be evaluated for an arbitrary configuration efficiently, and is thus well-suited for Monte
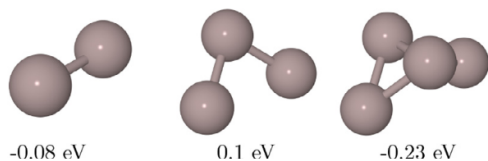

Fig. 1. Selected examples of clusters with the corresponding effective cluster interaction (ECI) values included.
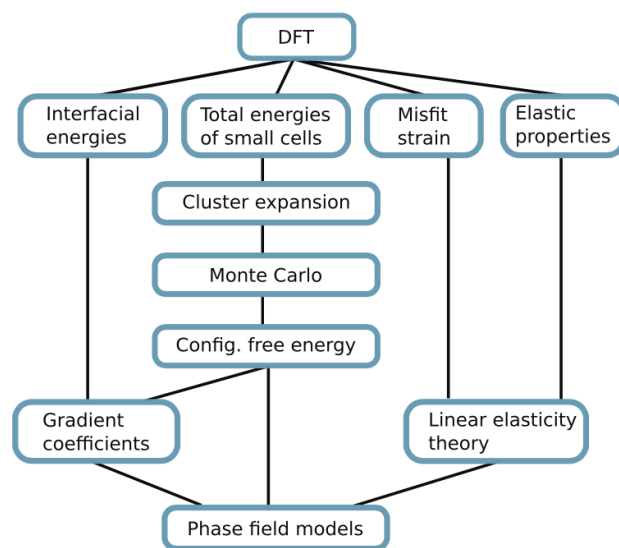
-0.08 eV   0.1 eV   -0.23 eV

Fig. 2. Hierarchical overview of the methods used to study Al−Mg−Si alloys. The process starts from DFT calculations, and the results are propagated through several layers until the final phase-field model is obtained.

Carlo sampling. Consequently, configurational thermodynamics of the ternary Al−Mg−Si system can be explored across a large composition range at various temperatures. The free energy of the system is of particular interest, as it determines stable phases. Monte Carlo calculations can be performed either at a fixed concentration or at a fixed chemical potential. In the latter case, the concentrations of the atomic species may vary while the overall number of atoms is fixed. The chemical potentials are subtracted from ECI corresponding to the singlet terms $V_{singlet}^{(k)} \to V_{singlet}^{(k)} - \mu_k$, where μ_k is the chemical potential associated with the basis function k.

The free energy as a function of composition and chemical potentials is easily obtained by performing MC calculations in one of the two ensembles above. However, it is also interesting to apply meta-dynamics MC sampling to obtain free energies as a function of arbitrary collective variables [21]. The free energy G as a function of a general collective variable Q^* is defined as

$$e^{-\beta G(Q^*)} = \sum_{\sigma} \delta\left(Q(\boldsymbol{\sigma}) - Q^*\right) e^{-\beta E(\boldsymbol{\sigma})}, \tag{3}$$

where $\beta = 1/k_B T$ is the Boltzmann factor, $Q(\sigma)$ is the value of the collective variable for a micro-state given by the occupation variables σ. The effect of the delta function is to suppress contributions from configurations that do not have the correct value for the collective variable. To map out the free energy landscape as a function of Q^*, the MC sampler needs to visit high energy regions. This is achieved by adding a bias potential $V(Q^*)$ to the energy, thus $E(\sigma) \to E(\sigma) + V(Q^*)$. By altering $V(Q^*)$, configurations with high energies (large $E(\sigma)$) can become favourable during the course of the simulation, and therefore, visited by the MC sampler.

By multiplying by $\exp(\beta G(Q^*))$ on both sides in Eq. (3) leads to

$$1 = \sum_{\sigma} \delta\left(Q(\boldsymbol{\sigma}) - Q^*\right) e^{-\beta\left(E(\boldsymbol{\sigma}) - G(Q^*)\right)}, \tag{4}$$

where the factor $\exp(\beta G(Q^*))$ can be taken inside the summation due to the delta function. The unknown free energy $G(Q^*)$ acts as a bias potential as explained above. As the sum in Eq. (4) is equal to one for all Q^*, all values of Q^* are equally likely. Hence, if one can find a bias potential such that all values Q^* occur with equal probability, one knows that this bias potential corresponds to the sought free energy $G(Q^*)$. In practice, we iteratively determine this bias potential. We

first partition the domain of possible Q^* values into bins and start with an initial guess for $V(Q^*)$; here we simply use a constant value. During the sampling, we maintain two histograms, one that tracks how many times a particular bin has been visited and one that represents $V(Q^*)$. We generate a random trial move which is either accepted or rejected, according to the Metropolis acceptance criteria. After the move, the current configuration will have a value Q_1 (if the move was rejected this is the same as the value before the move). The bin corresponding to Q_1 in the histogram of visits is incremented by a value 1. Similarly, the bin in the histogram representing V is incremented by a modification factor f. This process continues until the histogram of visits is flat. Here, we adopt the convention that a histogram is considered flat when the minimum value is greater or equal to 80% of the mean value. When the histogram of visits is flat, we erase it and start a new iteration with a smaller modification factor f. Note that in the second iteration we start from the previous estimate of $V(Q^*)$. Here, we started with $f = 1$ and reduced it stepwise by a factor 10 until it was 10^{-4} in the last run.

The above procedure allows us to investigate the stability of an ordered phase as a function of the degree of disorder. We are mainly interested in the layered MgSi phase and therefore define the degree of disorder via the normalised diffraction intensity of a reflection that is characteristic for the layers

$$S_k = \left| \langle \frac{1}{N} \sum_{i=1}^{N} \delta_{Mg}(\mathbf{r}) e^{i\mathbf{q}_k \cdot \mathbf{r}} \rangle \right| \tag{5}$$

where $\mathbf{q}_k$ is the reciprocal vector corresponding to a characteristic layering direction, N is the number of atoms and $\delta_{Mg}(\mathbf{r})$ is a function that is 1 if the symbol at position $\mathbf{r}$ in the MC cell is Mg and 0 otherwise. For a FCC phase with (100) planes, each Mg layer is separated by a distance $a = 4.05$Å. By choosing $\mathbf{q}_k = (2\pi/a, 0, 0)$, S_k becomes a measure of the thermal averaged degree of layering. Since we normalise by the overall number of atoms, S_k is equal to 0.5 for the perfectly ordered MgSi phase and approaches zero as the phase gets disordered.

2.2. Phase-field modelling

Phase-field methods have been successfully used to describe a large variety of nucleation processes [14,15,22]. In the following, we describe the necessary model needed to study a two-phase mixture, namely MgSi nuclei in an Al host material.

The total free energy of the composite is modelled by the sum of three terms

$$G_{tot} = G_{bulk} + G_{surf} + G_{el}, \tag{6}$$

where G_{bulk} is the bulk free energy, G_{surf} is the interfacial energy between the different phases and G_{el} is the elastic energy due to misfit strain which originates from the different stress-free lattice parameters for Al and MgSi. The misfit strain ϵ is defined via

$$\begin{aligned} C_{MgSi} &= P C_{Al} \\ \epsilon &= \frac{1}{2}(P^T P - I), \end{aligned} \tag{7}$$

where C represents a matrix where each column is a cell vector, P is a matrix that transforms the stress free unit cell of Al into the one of MgSi and I is the identify matrix.

Therefore, strain fields will be present in the vicinity of a precipitate. The energy associated with the strain fields is an additional energy cost that affects the precipitation process.

The two first terms in (6) are given by

$$G_{bulk} + G_{surf} = \int_V d^3\mathbf{r} \left(g(c,\{\eta_k\}) + \alpha |\nabla c|^2 + \sum_{ijk} \beta_{ij} \frac{\partial \eta_k}{\partial x_i} \frac{\partial \eta_k}{\partial x_j} \right), \tag{8}$$

where c is the concentration of MgSi, η_k is an order parameter that measures the orientation of the MgSi phase, $g(c,\{\eta_k\})$ is the free energy density and α and β_{ij} are gradient coefficients. The sum over all indices i, j and k runs from one to three. The energy associated with the formation of interfaces is captured by the gradient coefficients, which further can be obtained from the surface tension [23]. We model the misfit strain energy by using the homogeneous elastic modulus approximation [24].

In the present work, we wish to study several properties of the Al-MgSi system. First, to capture the diffusion of the initial phase separation, we define a current $\mathbf{j} = -M \nabla \mu$, where μ is given by the partial derivative of the free energy g with respect to the MgSi concentration c. Then we set the local rate of change of the concentration equal to the negative divergence of the current. The resulting differential equation is the Cahn−Hilliard equation [23]

$$\frac{\partial c}{\partial t} = M \nabla^2 \left(\frac{\partial g}{\partial c} - 2\alpha \nabla^2 c \right), \tag{9}$$

where M is the mobility. The second type of property we want to study by continuum models is the effect of strain fields and surface tensions *after* a GP zone is formed. Here, we add a set of auxiliary fields $\{\eta_k\}$ and incorporate the effect of surface tensions in the auxiliary fields

$$\frac{\partial c}{\partial t} = M \nabla^2 \frac{\partial g}{\partial c}, \tag{10}$$

$$\frac{\partial \eta_k}{\partial t} = -L \left(\frac{\partial g}{\partial \eta_k} - 2 \sum_{ij} \beta_{ij} \frac{\partial^2 \eta_k}{\partial x_i \partial x_j} + \frac{\delta G_{el}}{\delta \eta_k} + \lambda \frac{dh}{d\eta_k} \right), \tag{11}$$

where M and L are mobilities. Furthermore, we select L such that $M/L \Delta x = 1$, where Δx is the spatial discretization. The term $\lambda h'(\eta_k)$ in the last equation originates from a volume constraint imposed by a Lagrange multiplier

$$\mathcal{L}(\lambda, \eta_k) = \lambda \left(\int_V d^3\mathbf{r} h(\eta_k) - V_{prec} \right), \tag{12}$$

$$h(\eta_k) = \begin{cases} 1, & \eta_k \geq 1 \\ 3\eta_k^2 - 2\eta_k^3, & 0 < \eta_k < 1 \\ 0, \eta_k \leq 0 \end{cases} \tag{13}$$

where $h(\eta_k)$ is a smooth interpolating function whose integral represents the volume of the precipitate V_{prec}. λ is a time-dependent Lagrange multiplier that is determined such that the volume averaged value of η_k is constant [25,26].

We now proceed to describe how the free energies entering the aforementioned phase-field equations is parameterised. While parameterising the functions needed for Eqs. (10) and (11) we follow the former studies closely [15,22].

$$\begin{aligned} g(c, \eta_1, \eta_2) &= p(c) + A(c-c_0) \sum_k \eta_k^2 + p_4(\{\eta_k\}) + p_6(\{\eta_k\}), \\ p_4(\{\eta_k\}) &= B \sum_k \eta_k^4 + D \sum_{k \neq l} \eta_k^2 \eta_l^2 \\ p_6(\{\eta_k\}) &= C \sum_k \eta_k^6 + E \sum_{k \neq l} \eta_k^2 \eta_l^4 \end{aligned} \tag{14}$$

where $p(c)$ is a polynomial (see Appendix A).

First, it should be noted that the equilibrium value for η_k can be found by requiring that the derivatives with respect to η_k of $g(c, \eta_1, \eta_2, \eta_3)$ are zero. Hence, there are three equilibria $(\eta_1, \eta_2, \eta_3) = (0, 0, 0), (\eta_{eq}, 0, 0), (0, \eta_{eq}, 0)$ and $(0, 0, \eta_{eq})$, depending on the concentration c. The equilibrium value for η is given by

$$\eta_{eq}(c) = \pm \sqrt{-\frac{B}{3C} \pm \sqrt{\left(\frac{B}{3C}\right)^2 - \frac{A(c-c_0)}{3C}}}. \tag{15}$$

By carrying out the simulations to calculate the free energy as a function of concentration ($Q = c$ in Eq. (3)) and assuming that the

order parameters are slaved by the concentration, we can fit the function $g(c, \eta_{eq}, 0, 0)$. This allows us to determine the parameters A, B, C, c_0 and $p(c)$. The remaining coefficients D and E are fitted to the free energy curve as a function of varying degree of layering ($Q = S_k$ in Eq. (3)). However, a direct fit to the data may lead to a nonphysical model with meta-stable phases with more than one of the order parameters ($\{\eta_k\}$) different from zero. Consequently, the coefficients D and E have to obey certain constraints. First, since we know that there are minima on each η-axis, the lowest order cross-terms have to be positive ($D \geq 0$). Secondly, we apply the requirement that for any concentration c the free energy curve should be monotonically increasing along the line $\eta_1 = \eta_2$. By differentiating Eq. (14) with respect to η_1 this requirement is expressed by the in-equality

$$A(c-c_0) + 4B\eta_1^2 + 4D\eta_1^2 + 6C\eta_1^4 + 6E\eta_1^4 \geq 0 \qquad (16)$$

We now proceed to formulate a set of linear constraints on the coefficients D and E which can easily be applied to a fitting algorithm. First, when η_1 is large the quartic terms will dominate and the constraint reduces to $E \geq -C$. For small values of η_1, the quadratic term dominates and the most strict constraint is $D \geq -B - \min_c\{A(c-c_0)\}$, where the last term should be minimised over all concentrations $c \in [0, c_0]$. If A is negative, the result of the minimisation is $c = c_0$, and for positive A it is $c = 0$.

To complete the phase-field description of the Al-MgSi system, the gradient coefficients need to be determined. We limit ourselves to the case where β_{ij} is diagonal. Furthermore, the system we study has only two distinct surfaces. Consequently, we choose $\alpha = 0$. This leaves us with two unknown gradient coefficients, β_{11} and β_{22}. Following Cahn [23], the gradient coefficients are related to the interfacial energy γ by

$$\gamma = \int_{x_0}^{x_1} dx \sqrt{\kappa \Delta g(x)}, \qquad (17)$$

where x is an arbitrary field variable characterising the free energy and κ their corresponding gradient coefficient. $\Delta g(x)$ is the surface formation energy, x_0 and x_1 are the values for the integration variables on each side of the dividing surface, respectively. For the two unknowns, β_{11} and β_{22} two interfacial energies are needed. We select an interface between Al and MgSi where the layer normal is parallel to the interface and another one where it is perpendicular. We integrate along the order parameter η, and let the concentration vary according to $\partial g/\partial c = 0$. The concentration thus becomes a function of the order parameter

$$\gamma_\perp = \int_0^{\eta_{eq}} d\eta \sqrt{\beta_{11} \Delta g\big(c(\eta), \eta\big)}, \qquad (18)$$

$$\gamma_\parallel = \int_0^{\eta_{eq}} d\eta \sqrt{\beta_{22} \Delta g\big(c(\eta), \eta\big)}, . \qquad (19)$$

During the initial coarsening process, we do not take into account the effect of strain fields and surface anisotropy. It is thus sufficient to solve Eq. (9) and the free energy entering is obtained by a direct polynomial fit to the free energy as a function of concentration. The gradient coefficient α is obtained by a slight modification of Eq. (19) where we take the interfacial energy to be the average of $\gamma_\perp$ and $\gamma_\parallel$.

Equipped with a parameterised phase-field model from CE and DFT, quantitative information of the size distribution can be obtained by tracing the radially averaged Fourier transformed correlation function

$$\begin{aligned} F(\mathbf{r}, t) &= \int d^3r' c(\mathbf{r}+\mathbf{r}', t) c(\mathbf{r}', t) \\ P(k, t) &= \int d\Omega \mathcal{F}\{F(\mathbf{r}, t)\}, \end{aligned} \qquad (20)$$

where k and $d\Omega$ are the radius and the solid angle in reciprocal space, respectively. There are several ways of identifying one characteristic length scale at time t, but here we use the definition

$$L(t) = \frac{2\pi}{\int_0^\infty dk k^3 P(k, t)}. \qquad (21)$$

3. Computational methods

The cluster expansion model was fitted to 288 DFT calculations obtained with the GPAW program [27,28] in-plane wave mode using an energy cutoff at 600 eV and a k-point density of 5.4Å^{-3}. We relaxed the internal atomic positions and the cell sides in all cases, and we did not remove any structures from the training set, independent of the magnitude of the relaxations. We obtained a leave-one-out cross-validation score of 15 meV/atom by including clusters up to four atoms and fourth nearest neighbours in the cluster pool. The CE calculations were carried out with the CLEASE package [29] using a training set with cell sizes up to 64 atoms.

Our fitting procedure for mapping MC free energy curves to the functional form (14) was carried out as follows. First, we calculated $p(c)$, A, B and C by a direct fitting to the free energy curve. During this stage, η_k are assumed to take their equilibrium value. The model has a clear interpretation only when one of the auxiliary variables η_k is different from zero. Therefore, the remaining constants D and E, were chosen such that the free energy minima were located at (η_1, η_2, η_3) = $(\eta_{eq}, 0, 0)$, $(0, \eta_{eq}, 0)$ and $(0, 0, \eta_{eq})$.

The phase-field calculations used the Mesoscale Microstructure Simulation Project (MMSP) as the computational engine [30]. In this work, we studied Al−Mg−Si with two phase-field calculations. First, we studied the initial phase segregation through the Cahn-Hilliard model. The effect of interface anisotropy and strain fields was then studied by coupling a set of auxiliary fields to the model.

4. Results

The formation energy from DFT as a function of Mg concentration is shown in Fig. 3 and it shows stable phases at 0.25 (AlMgSi$_2$), 0.5 (MgSi) and 0.75 (Mg$_3$Si). The predictions of the same data set from the fitted CE model are included as open squares in the figure. The silicon concentration is restricted to remain less than 0.5 throughout the data set. At Mg concentrations close to 0.5, the CE model predicts the formation energy of MgSi to be slightly lower than the DFT reference. Furthermore, our CE model shows some deviation in predicting the formation energy of the AlMgSi$_2$ structure. However, we are primarily interested in the free energy landscape near pure Al and the vicinity of the MgSi phase.
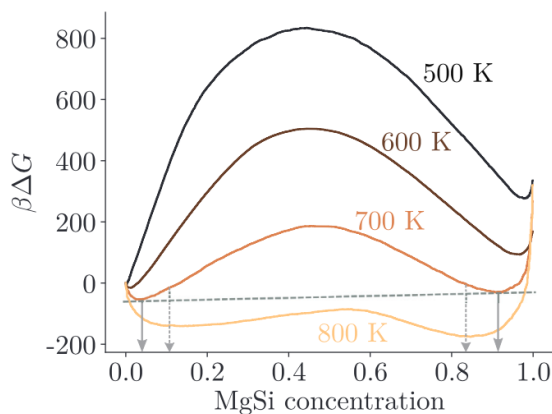
The free energy of the Al$_{2-2x}$Mg$_x$Si$_x$ system as a function of concentration and temperature was calculated by MC sampling and is shown in Fig. 4. The curves represent the difference in free energy relative to the value of pure Al. In all cases, local minima representing stable phases are seen at both low concentrations (Al phase) and high concentrations (MgSi). As the temperature is increased, the barrier separating the two phases decreases and eventually the two minima coalesce and the systems enter in a random phase. The solid lines in the corresponding phase diagram in Fig. 4(b) are found by locating the concentrations at which the free energies in the two phases have a common tangent. The shaded areas represent pure phases where the minority species are dispersed within the host material. The spinodal lines are obtained by locating inflection points on the free energy curves.

The free energy cost associated with introducing layering defects in the MgSi phase was calculated via meta-dynamics MC sampling, where the order parameter in Eq. (5) was used as the collective
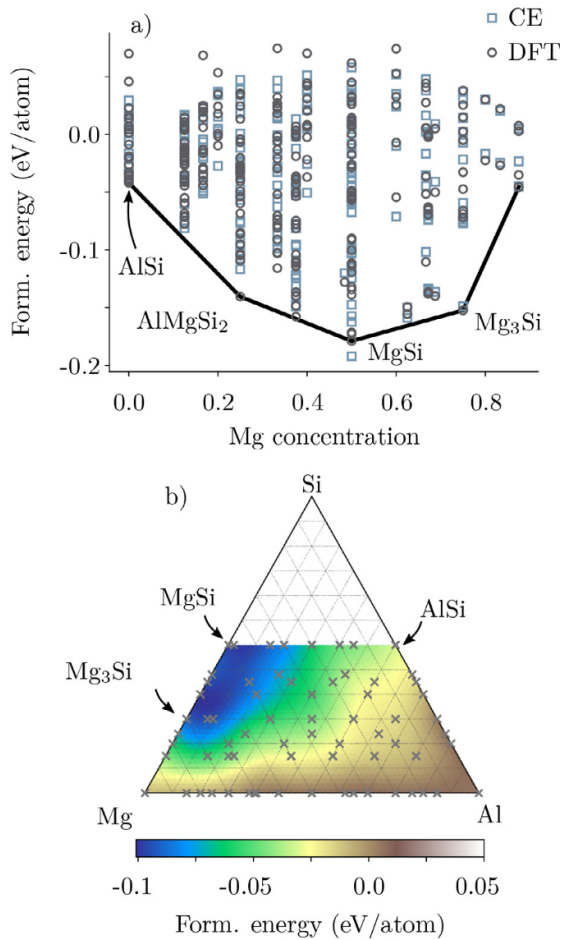
Fig. 3. (a) Formation energy from DFT calculations (circles) and CE predictions of the same structures (squares). (b) Distribution of the DFT training points on the ternary map. The formation energy is represented by colors, which are obtained via interpolation with respect to the DFT points. Note that the number of points in (b) appears fewer than in (a) because the training set includes several configurations for each concentration. (For interpretation of the references to color in this figure legend, the reader is referred to the web version of this article.)

variable. Fig. 5 shows the free energy curves at 600 K, 700 K and 800 K. As the simulation cell is half-filled with Mg atoms, the order parameter S_k in Eq. (5) is equal to 0.5 for a perfectly layered structure.

Fig. 4. (a) Free energy curves at four temperatures for the $Al_{2-2x}Mg_xSi_x$ system. The common tangent and the concentration of the inflection points are shown as examples. (b) Corresponding phase diagram.
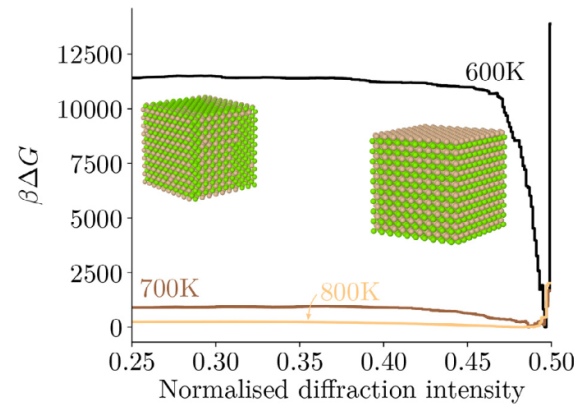

Fig. 5. Free energy cost associated with introducing defects in the layered MgSi phase. The normalised diffraction intensity is given by Eq. (5). The solid lines represents MC calculations at 600K, 700K and 800K, respectively.

At lower values, the MgSi phase exhibits its characteristic layered structure with defects, as illustrated by the inset geometries. We observe that the free energy cost associated with introducing layering defects decreases with increasing temperature. At sufficiently high temperatures the layered phase will no longer be stable, and the minimum near $\eta = 0.5$ vanishes. From the magnitude of the free energy at 600 K, we conclude that observing Si atom defects in the Mg layer and vice versa is unlikely.

The interfacial energies $\gamma_{\parallel}$ and $\gamma_{\perp}$ are displayed in Fig. 6 and they were obtained from the slope point of a linear fit to DFT slab calculations of different layer thicknesses [31]. The lowest interfacial energy is obtained for the case where the Al facing Mg and Si layers are alternating. We note that since periodic boundary conditions were used, $\gamma_{\perp}$ represents the average value for Al-Mg and Al-Si interfaces.

The initial phase separation process was modelled by the single Cahn−Hilliard Eq. (9) without the auxiliary fields in Eq. (11). The free energy input was a 10th order polynomial fitted to the free energy at 600 K in Fig. 4. The simulation cell was initialised by a random concentration field. The evolution of the radial averaged Fourier transform of the concentration pair correlation function (Eq. (20)) is shown in Fig. 7(a). In the beginning, a wide range of spatial frequencies are present, but as the system evolves towards equilibrium the lower frequencies get an increasingly strong signal. Except for a short time at the very beginning of the coarsening process, the mean spatial frequency (Fig. 7b) follows a power law for all concentrations, with a dynamic exponent of –0.24, which is very close to $-\frac{1}{4}$. These findings are consistent with previous studies of the Cahn−Hilliard
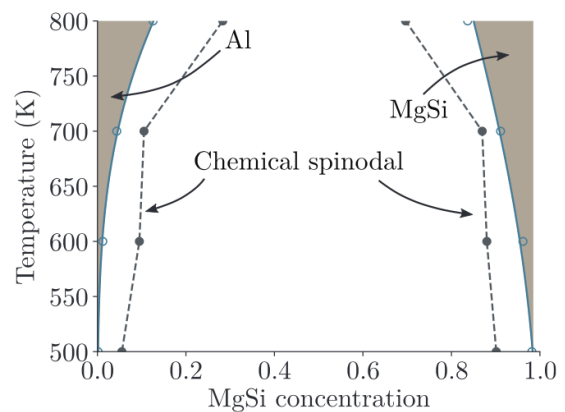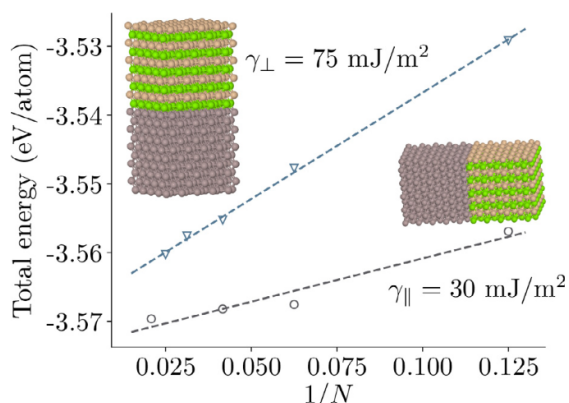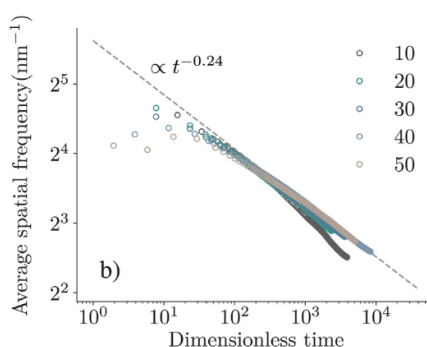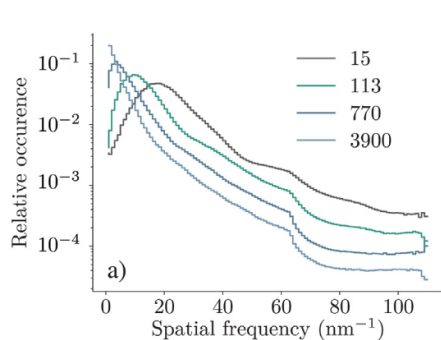
Fig. 6. Calculated DFT interface energies for the two surfaces shown where the normal vector to the Mg−Si planes is normal and parallel to the interface, respectively. The interface energy is extracted from the slope of the curve $2A\gamma$, where A is the surface area.

Fig. 8. Scaled Fourier transformed correlation function at different times.

Table 1
Non-zero components (Mandel notation) of the elastic tensor of the Al and MgSi phases.

Component	Value (GPa)	Phase
$C_{11} = C_{22} = C_{33}$	100	Al
$C_{12} = C_{13} = C_{23}$	60	Al
$C_{44} = C_{55} = C_{66}$	67	Al
$C_{11} = C_{33}$	75	MgSi
C_{22}	121	MgSi
$C_{12} = C_{32}$	46	MgSi
$C_{21} = C_{23}$	34	MgSi
$C_{13} = C_{31}$	53	MgSi
$C_{44} = C_{55} = C_{66}$	30	MgSi

equation when interface-diffusion controls the coarsening dynamics [32]. In Appendix C, we show that the dynamical exponent remains unchanged if one includes anisotropy in the surface tensions. The characteristic size L, given by the inverse of the average spatial frequency, therefore evolves as $L \sim \sqrt[4]{t}$. An illustration of the spontaneous phase separation process at 80% Al is shown in Fig. 7(c).
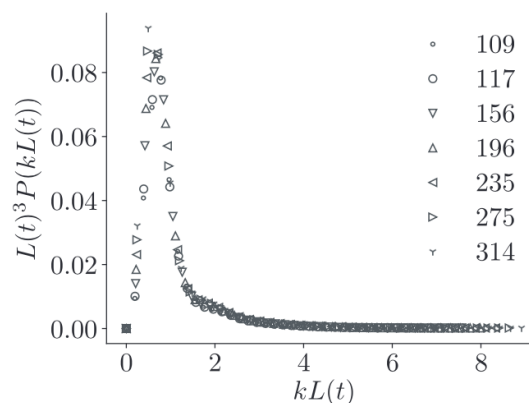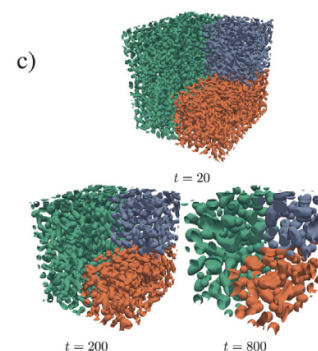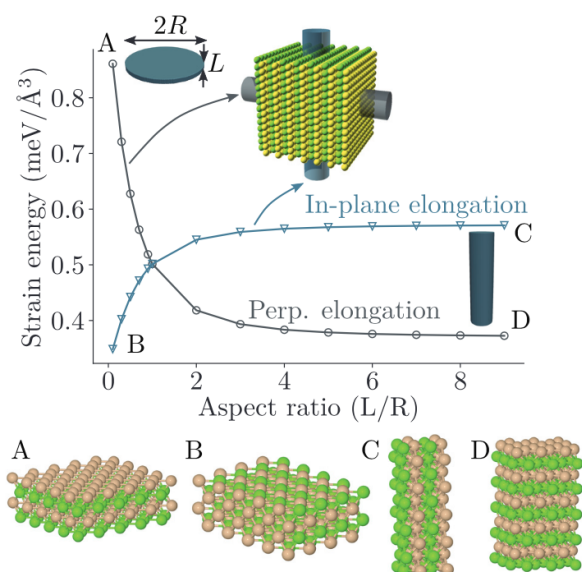
Further, if the coarsening is in the scaling regime, all curves $P(k, t)$ at different times and spatial frequencies should collapse onto the same curve if plotted appropriately. We expect the function $L(t)^3 P(kL(t))$ to overlap for different times (Fig. 8) where P is defined in Eq. (20). Using the characteristic length scale derived from the average spatial frequency, we indeed confirm that the distribution of length scales exhibits scaling behaviour when the Cahn−Hilliard equation is solved based on the free energy curve showed in Fig. 4(a).

The misfit strain of the layered MgSi phase when embedded in an Al host was found from DFT calculations to be $\epsilon_{xx} = \epsilon_{zz} = 0.044$, $\epsilon_{yy} = -0.028$, $\epsilon_{xy} = \epsilon_{yz} = 3 \times 10^{-4}$ and $\epsilon_{xz} = 8.6 \times 10^{-4}$. The plane normal vector was oriented along the y-axis, leading to the MgSi structure being stretched in the direction normal to the layers while experiencing in-plane compression. The elements of the elastic tensors in Mandel notation are given in GPa in Table 1.

The effect of strain fields due to the lattice mismatch between MgSi and Al within the homogeneous modulus approximation is shown in Fig. 9. We consider two limiting orientations where the base circle of the cylinder lies in the MgSi planes (cut 1) or perpendicular (cut 2). Interestingly, the dependence on the aspect ratio is

rather different. In cut 1, the strain energy decreases with increasing aspect ratio, meaning that needle-like inclusions have a lower strain energy. For cut 2 the situation is opposite, such that plate-like inclusions yield the lowest strain energy. Further, we note that the minimum strain energy for cut 2 is marginally lower than that of the needle-like inclusion for cut 1.

The effect of surface energetics and strain energies was studied by employing a phase-field model based on the 700 K-curve in Fig. 4. We investigated the time evolution of several MgSi domains as shown in Fig. 10. Initially, 20 precipitates were randomly distributed with the constraint that they should be at least 4.5 nm apart. The size of the precipitates were 4.5nm × 4.5nm, leading to an Al concentration of ∼ 92%. The initially square-like precipitates evolve towards needle-shaped objects. Furthermore, the number of precipitates decreases favouring large precipitates. The coarsening occurs via two

Fig. 7. (a) Radially averaged Fourier transformed concentration field at dimensionless times 15, 113, 770 and 3900. (b) Time evolution of the average spatial frequency at various solute concentrations and (c) Visualisation of the coarsening process. The colors are included for visual clarity. (For interpretation of the references to color in this figure legend, the reader is referred to the web version of this article.)

129

Fig. 9. Strain energy of the MgSi phase included in an Al host matrix within the homogeneous modulus approximation. The aspect ratio L/R, shown in the upper left inset, increases along the abscissa. The upper right inset shows the cut direction at which the volume of the MgSi phase is cut and inserted into the Al host. *Perp. elongation* refers to elongation along the normal vector of the planes and *in-plane elongation* refers to elongation parallel to the planes. Illustrations of the atomic arrangements at four limiting points (A, B, C, and D) are shown at the bottom.

mechanisms. First, we observe Ostwald ripening [33] where the smallest precipitates dissolve and the atoms diffuse to larger ones. Secondly, precipitates coalesce when they meet while having the same layering direction.

5. Discussion

We have shown above that by a systematic investigation of the energy costs of a layered MgSi phase within an aluminium host, the preferred domain shape can be predicted. First, the free energy cost associated with the configurational disorder in the layered MgSi phase was studied (Fig. 5). At temperatures lower than 700 K, the energy cost associated with layering defects is substantial. Hence, we conclude that defects within the MgSi phase at the temperatures of interest are highly unlikely. This observation justifies the major simplification where we only consider interface energies and elastic energies of the perfectly ordered MgSi phase.

The surface energies were obtained by considering two distinct faces; one where a layer with only one atom type is interfacing the host, and one where alternating layers of the two species comprise an interface with the host. We find that the energy associated with an interface of only one species is approximately twice as high as the energy of forming a surface with alternating layers. Thus, by only
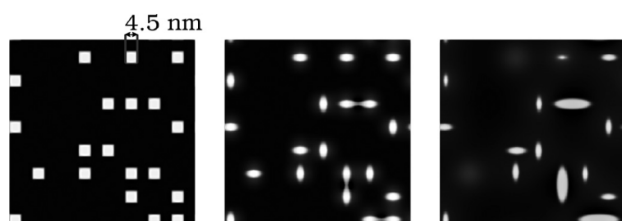
Fig. 10. Phase-field calculation of the time evolution of MgSi precipitates.

considering interface energies, the MgSi precipitate prefers to increase the surface area for alternating layers.

The elastic strain energies of MgSi are minimised for a plate-like shape (Fig. 9). However, the strain energy of a needle with alternating layers is only marginally larger than that of the platelet. For small GP zones, interfacial energies will dominate the strain energies. Hence, GP zones that are slightly elongated along the atomic plane normal have the lowest energy. As the GP zones grow, the elastic energy will become increasingly important. However, the MgSi domain is already elongated along the plane normals, which results in a high energy barrier associated with a transition into a plate-like shape. In contrast, the GP zone can continue to grow as a needle without any barrier. The result is that the MgSi GP zones become needle-shaped.

In the following, we proceed to estimate the impact of the different energy terms in the phase-field models. From Fig. 4, we find that the energy of a solid solution is several hundred times the thermal energy (kT). Consequently, in the early stages, there is a strong thermodynamical force that drives the system towards a phase-separated mixture. When a domain of MgSi has formed, the other energy terms become important. The strain energy scales linearly with the volume of the domain, while the interfacial energies increases linearly with the surface area of the domain. A typical size at which these two terms are of the same order of magnitude is obtained by considering a spherical shaped domain. From Fig. 9 we see that the strain energy for a spherical precipitate is approximately $E_{\text{elast}} \approx 0.5$ meV/Å^3. The average surface tension is $\overline{\gamma} \approx 50$ mJ/$\text{m}^2 \approx 3$meV/Å^2. The size at which strain energy is equal to the interfacial energy is a measure of the size at which strain energies start to dominate. For a spherical particle, the critical radius is $r_c = 3\overline{\gamma}/\Delta E_{\text{elast}} = 1.8$nm.

Interestingly, plate-like GP zones have experimentally been observed by Matsuda et al. [34], who proposed that the GP zones of the MgSi phase are platelets of diameter 30 nm and thickness of 2.5 nm. The atomic planes within the observed structure are characterised by each element being surrounded by four sites of the opposite kind, shown as plate B in Fig. 9. We note that the GP zone observed by Matsuda et al. is the one that has the lowest elastic energy. Further, Matsuda et al. proposed a growth mechanism where multiple GP zones aggregate and form a needle-shaped domain. Based on our multi-scale calculations, we conclude that the plate-like GP zones can be observed because of the small elastic fields associated with them. Moreover, the observed tendency to aggregate into needle-like GP zones can be explained by a combination of forming favourable interfaces within the Al host and the low elastic energies connected to a needle-like GP zone. In conclusion, MgSi domains tend to develop towards structure D in Fig. 9.

For high strength aluminium alloys, the formation of β'' precipitates is crucial. The β''-eye [3], characterised by one Mg atom being shifted by 1/2 lattice parameter, is a precursor to the fully developed β'' precipitate (see Appendix B). The translation of an entire Mg column seems geometrically unnatural for any other domain shapes than needles. In this work, we have established that the shape of the MgSi FCC phase is indeed needle-like. Consequently, a growth mechanism where the MgSi FCC phase is a precursor of the β'' precipitate is feasible.

In summary, our calculations suggest the following initial steps of the β'' precipitation process. First, Mg and Si form small and slightly elongated atomic clusters caused by interfacial energies. As the clusters grow, a combination of surface energetics and strain energetics leads to needle-shaped domains. Geometrically, this is a feasible state for promoting continued vacancy-assisted transitions into pre-β'' and finally to larger β'' precipitates.

6. Conclusion

We have developed a multi-scale modelling approach (DFT, MC, phase-field) for investigating the formation of MgSi precipitates in

the FCC Al host matrix. At the atomistic scale, we have trained a cluster expansion model based on DFT calculation of benchmark structures to obtain a fitted expression for configurational energy. The CE model is coupled with Monte Carlo calculations, where we identify that the layered MgSi phase is particularly stable. Further, the interface energetics of Al-MgSi and elastic properties have been calculated via DFT. Finally, we have incorporated all the information from atomistic simulation (DFT, MC) in a mesoscale phase-field model.

The simulations of many small precipitates (Fig. 10) show a tendency to form elongated domains. Moreover, we find that precipitates grow by two distinct mechanisms; Ostwald ripening and coalescence of precipitates with equal layering orientation. The observation that MgSi domains on the FCC lattice tend to be needle-like demonstrates that this phase is a natural precursor for the important β'' precipitate which is also known to be needle-like.

In this work, we made at least two approximations that will serve as starting points for future work. First, we did not take into account the fact that Mg and Si diffuse at different rates. Incorporating different mobilities of the two species can help to understand the early composition evolution of the precipitates. On a longer time scale, misfit strains will also depend on the composition. Consequently, both small amounts of Al and slightly different Mg/Si ratio can affect the elastic energies. Thus, extending the models presented here to take into account composition-dependent misfit strains will potentially give new insight into the compositional evolution of precipitates in aluminium alloys.

Finally, we note that all parameters apart from the kinetic parameters (such as mobilities) were obtained from first-principles data. The atomic mechanisms for the diffusion process, including the role of vacancies, require kinetic Monte Carlo simulations and will be a topic of future work.

Declaration of Competing Interest

The authors declare that they have no known competing financial interests or personal relationships that could have appeared to influence the work reported in this paper.

Acknowledgments

Appendix A. Phase-field model coefficients

The explicit form of the polynomial in Eqs. (10) and (11) is

$$g(c, \eta_1, \eta_2) = 1.57c^2 - 0.09c - 0.08 \\ -4.16c(\eta_1^2 + \eta_2^2) + 3.77(\eta_1^2 + \eta_2^2) \\ -8.29(\eta_1^4 + \eta_2^4 - \eta_1^2\eta_2^2 - \eta_1^6 - \eta_2^6) \\ -2.76(\eta_1^2\eta_2^4 + \eta_1^4\eta_2^2)$$

Fig. A.11 shows the form of this function in the (c, η_1)-plane. It displays two local minima, one at pure Al and one for layered MgSi, which coincide with the atomistic results in Figs. 4 and 5.

Appendix B. Misfit strain of β''-eye

The transition from the MgSi FCC phase to the β''-eye, consists of one column of Mg atoms moving into the Si layer. The resulting misfit strain is
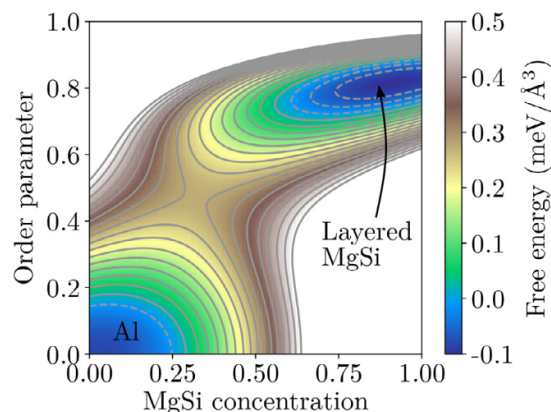

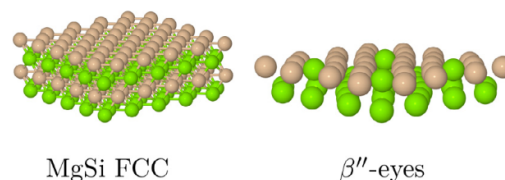**Fig. A.11.** Free energy resulting from the parameterised expression $g(c, \eta_1, \eta_2)$, when $\eta_2 = 0$.

Fig. B.12. *Left*: MgSi FCC phase characterised by alternating layers of Mg and Si. *Right*: β''-eyes where some Mg atoms are shifted into the Si layers.

$$\epsilon^* = \begin{bmatrix} 6.3 \times 10^{-2} & 0 & 3 \times 10^{-7} \\ 0 & -6.8 \times 10^{-5} & 0 \\ 3 \times 10^{-7} & 0 & 6.3 \times 10^{-2} \end{bmatrix}. \tag{B.1}$$

Most notably there is almost no strain in the direction orthogonal to the plane. Consequently, the needle-shaped MgSi FCC phase can

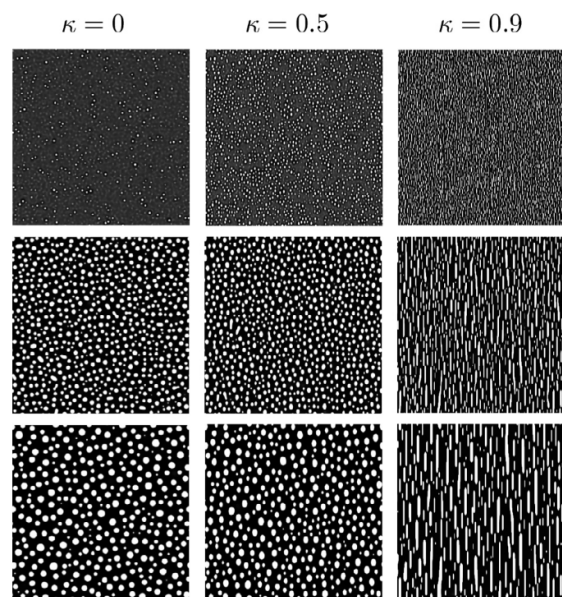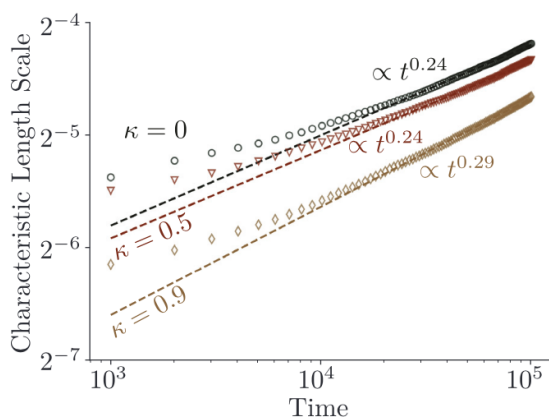**Fig. C.13.** Evolution of the same initial concentration distribution at different values of the global anisotropy coefficient κ.

131

Fig. C.14. Time evolution of the characteristic length scale for different values of the global anisotropy parameter κ.

further lower the energy by shifting one column of Mg atoms into the Si layer as seen in Fig. B.12.

Appendix C. CH equation with a global anisotropy

In the discussion on the initial separation process, we made the approximation of neglecting anisotropy in the surface tension. Here, we explore the effect of this approximation by showing that the growth law is unaltered under a global anisotropy. We consider the equation

$$\frac{\partial c}{\partial t} = M \nabla^2 \left(\frac{\partial g}{\partial c} - 2\alpha_x \frac{\partial^2 c}{\partial x^2} - 2\alpha_y \frac{\partial^2 c}{\partial y^2} \right) \tag{C.1}$$

By introducing a global anisotropy function $\kappa = 1 - \alpha_y / \alpha_x$ Eq. (C.1) becomes

$$\frac{\partial c}{\partial t} = M \nabla^2 \left(\frac{\partial g}{\partial c} - 2\alpha_x \nabla^2 c - 2\kappa\alpha_x \frac{\partial^2 c}{\partial y^2} \right). \tag{C.2}$$

We note that (C.2) is equal to Eq. (9) apart from the last term. We performed a series of calculations for $\kappa = 0, 0.5$ and 0.9 (Fig. C.13) and calculated the time evolution of the characteristic length scale $L(t)$.

When $\kappa = 0.5$ the phases being formed are only slightly elongated along one axis. Only in the extreme case of $\kappa = 0.9$ we observe a strong elongation of the structure. Thus, the global anisotropy has only a rather weak effect on the calculated growth rate (Fig. C.14).

By studying the solution of the Cahn−Hilliard equation under a global anisotropy, we see that the exact shape of the formed phases has a marginal effect on the dynamic exponents. This observation suggests that anisotropy in the surface tensions has a negligible effect in the early stages of the phase separation process.

References

[1] E.A. Starke, J.T. Staley, Application of modern aluminum alloys to aircraft, Prog. Aerosp. Sci. 32 (2−3) (1996) 131−172.

[2] D. Carle, G. Blount, The suitability of aluminium as an alternative material for car bodies, Mater. Des. 20 (5) (1999) 267−272.

[3] C.D. Marioara, S.J. Andersen, J. Jansen, H.W. Zandbergen, Atomic model for gp-zones in a 6082 Al−Mg−Si system, Acta Mater. 49 (2) (2001) 321−328.

[4] J.P. Lynch, L.M. Brown, M.H. Jacobs, Microanalysis of age-hardening precipitates in aluminium alloys, Acta Metall. 30 (7) (1982) 1389−1395.

[5] J.M. Sanchez, Cluster expansions and the configurational energy of alloys, Phys. Rev. B 48 (18) (1993) 14013.

[6] A. van de Walle, G. Ceder, Automating first-principles phase diagram calculations, J. Phase Equilibria 23 (4) (2002) 348.

[7] V. Blum, A. Zunger, Mixed-basis cluster expansion for thermodynamics of BCC alloys, Phys. Rev. B 70 (15) (2004) 155108.

[8] J.G. Goiri, A. Van der Ven, Phase and structural stability in ni-al systems from first principles, Phys. Rev. B 94 (9) (2016) 094111.

[9] M. Asta, V. Ozolins, C. Woodward, A first-principles approach to modeling alloy phase equilibria, JOM 53 (9) (2001) 16−19.

[10] C. Wolverton, First-principles theory of 250 000-atom coherent alloy microstructure, Modell. Simul. Mater. Sci. Eng. 8 (3) (2000) 323.

[11] D. Kleiven, O.L. Ødegård, K. Laasonen, J. Akola, Atomistic simulations of early stage clusters in AlMg alloys, Acta Mater 166 (2019) 484−492.

[12] R. Kobayashi, D. Giofré, T. Junge, M. Ceriotti, W.A. Curtin, Neural network potential for Al-Mg-Si alloys, Phys. Rev. Mater. 1 (5) (2017) 053604.

[13] S.J. Andersen, H.W. Zandbergen, J. Jansen, C. Traeholt, U. Tundal, O. Reiso, The crystal structure of the β phase in Al−Mg−Si alloys, Acta Mater. 46 (9) (1998) 3283−3298.

[14] N. Moelans, B. Blanpain, P. Wollants, An introduction to phase-field modeling of microstructure evolution, Calphad 32 (2) (2008) 268−294.

[15] D.Y. Li, L.Q. Chen, Computer simulation of stress-oriented nucleation and growth of $\theta\check{U}$ precipitates lnal−Cu alloys, Acta Mater. 46 (8) (1998) 2573−2585.

[16] V. Vaithyanathan, C. Wolverton, L.Q. Chen, Multiscale modeling of $\theta\check{U}$ precipitation in al−cu binary alloys, Acta Mater. 52 (10) (2004) 2973−2987.

[17] H. Liu, Y. Gao, J.Z. Liu, Y.M. Zhu, Y. Wang, J.F. Nie, A simulation study of the shape of β' precipitates in Mg−y and Mg−Gd alloys, Acta Mater. 61 (2) (2013) 453−466.

[18] S. DeWitt, E.L.S. Solomon, A.R. Natarajan, V. Araullo-Peters, S. Rudraraju, L.K. Aagesen, B. Puchala, E.A. Marquis, A. Van Der Ven, K. Thornton, et al., Misfit-driven β' precipitate composition and morphology in Mg-Nd alloys, Acta Mater. 136 (2017) 378−389.

[19] A. van de Walle, Multicomponent multisublattice alloys, nonconfigurational entropy and other additions to the alloy theoretic automated toolkit, Calphad 33 (2) (2009) 266−278.

[20] L.J. Nelson, V. Ozoliņš, C.S. Reese, F. Zhou, G.L.W. Hart, Cluster expansion made easy with Bayesian compressive sensing, Phys. Rev. B 88 (15) (2013) 155105.

[21] D. Chandler, Introduction to modern statistical mechanics, in: D. Chandler (Ed.), Introduction to Modern Statistical Mechanics, Oxford University Press, 1987, p. 288.Sep 1987. ISBN-10: 0195042778. ISBN-13: 9780195042771

[22] V. Vaithyanathan, C. Wolverton, L.Q. Chen, Multiscale modeling of precipitate microstructure evolution, Phys. Rev. Lett. 88 (12) (2002) 125503.

[23] J.W. Cahn, J.E. Hilliard, J. Chem. Phys. 28 (1958) 258.

[24] A.G. Khachaturyan, S. Semenovskaya, T. Tsakalakos, Elastic strain energy of inhomogeneous solids, Phys. Rev. B 52 (22) (1995) 15909.

[25] H. Garcke, B. Nestler, B. Stinner, F. Wendler, Allen−Cahn systems with volume constraints, Math. Models Methods Appl. Sci. 18 (08) (2008) 1347−1381.

[26] B. Bhadak, R. Sankarasubramanian, A. Choudhury, Phase-field modeling of equilibrium precipitate shapes under the influence of coherency stresses, Metall. Mater. Trans. A 49 (11) (2018) 5705−5726.

[27] J.J. Mortensen, L.B. Hansen, K.W. Jacobsen, Real-space grid implementation of the projector augmented wave method, Phys. Rev. B 71 (3) (2005) 035109.

[28] J.E. Enkovaara, C. Rostgaard, J.J. Mortensen, J. Chen, M. Dułak, L. Ferrighi, J. Gavnholt, C. Glinsvad, V. Haikola, H.A. Hansen, et al., Electronic structure calculations with GPAW: a real-space implementation of the projector augmented-wave method, J. Phys.: Condens. Matter 22 (25) (2010) 253202.

[29] J.H. Chang, D. Kleiven, M. Melander, J. Akola, J.M.G. Lastra, T. Vegge, Clease: a versatile and user-friendly implementation of cluster expansion method, J. Phys.: Condens. Matter (2019).

[30] T. Keller, D. Lewis, pdetwiler44, YixuanTan, fields4242, lauera, and Zhyrek. mesoscale/mmsp: Zenodo integration, 2019, 10.5281/zenodo.2583258

[31] V. Fiorentini, M. Methfessel, Extracting convergent surface energies from slab calculations, J. Phys.: Condens. Matter 8 (36) (1996) 6525.

[32] J. Zhu, L. Chen, J. Shen, V. Tikare, Coarsening kinetics from a variable-mobility Cahn−Hilliard equation: application of a semi-implicit fourier spectral method, Phys. Rev. E 60 (4) (1999) 3564.

[33] J.V. Alemán, A.V. Chadwick, J. He, M. Hess, K. Horie, R.G. Jones, P. Kratochvíl, I. Meisel, G. Mita I.and Moad, et al., Definitions of terms relating to the structure and processing of sols, gels, networks, and inorganic-organic hybrid materials (IUPAC recommendations 2007), Pure Appl. Chem. 79 (10) (2007) 1801−1829.

[34] K. Matsuda, S. Ikeno, H. Gamada, K. Fujii, Y. Uetani, T. Sato, A. Kamio, High-resolution electron microscopy on the structure of Guinier-Preston zones in an al-1.6 mass Pct Mg 2 Si alloy, Metall. Mater. Trans. A 29 (4) (1998) 1161−1167.